AGU
ADVANCING EARTH AND SPACE SCIENCES

JGR Solid Earth

Key Points:

- We present a physics-informed deep learning eikonal tomography method for anisotropic velocity modeling
- The algorithm incorporates wave physics to simultaneously process multi-frequency data, ensuring reliable tomographic models
- We successfully recover the anisotropic velocity structure of the northeastern Tibet using less data than in traditional models

Correspondence to:

S. A. L. de Ridder and Y. Chen,
s.deridder@leeds.ac.uk;
johnyc@sustech.edu.cn

Physics-Informed Neural Networks for Elliptical-Anisotropy Eikonal Tomography: Application to Data From the Northeastern Tibetan Plateau

Yunpeng Chen[1,2] , **Sjoerd A. L. de Ridder[2]** , **Sebastian Rost[2]** , **Zhen Guo[1]** , **Xiaoyang Wu[1]** , **Shilin Li[1]** , and **Yongshun Chen[1]**

[1]Department of Ocean Science and Engineering, Southern University of Science and Technology, Shenzhen, China, [2]School of Earth and Environment, University of Leeds, Leeds, UK

Abstract We develop a novel approach for multi-frequency, elliptical-anisotropic eikonal tomography based on physics-informed neural networks (pinnEAET). This approach simultaneously estimates the medium properties controlling anisotropic Rayleigh waves and reconstructs the traveltimes. The physics constraints built into pinnEAET's neural network enable high-resolution results with limited inputs by inferring physically plausible models between data points. Even with a single source, pinnEAET can achieve stable convergence on key features where traditional methods lack resolution. We apply pinnEAET to ambient noise data from a dense seismic array (ChinArray-Himalaya II) in the northeastern Tibetan Plateau with only 20 quasi-randomly distributed stations as sources. Anisotropic phase velocity maps for Rayleigh waves in the period range from 10–40 s are obtained by training on observed traveltimes. Despite using only about 3% of the total stations as sources, our results show low uncertainties, good resolution and are consistent with results from conventional tomography.

Plain Language Summary Anisotropy refers to the directional dependence of seismic wave velocities, which can arise from a variety of factors such as crystal alignment, stress fields, or fluid-filled cracks. Elliptical-anisotropic eikonal tomography is a variant of eikonal tomography that can be used to estimate medium properties and reconstructed traveltimes from ambient noise data. In this study, we propose a new algorithm to implement multi-frequency, elliptical-anisotropic eikonal tomography based on physics-informed neural networks (pinnEAET), which combine data-driven models with theory-based models that include physics constraints on the system. We apply this architecture to data from a dense seismic array deployed on the northeastern Tibetan Plateau. Our results can achieve at least the same resolution as traditional methods while requiring less traveltime data. This strategy can provide new insights into the seismic imaging in case of limited or noisy data.

1. Introduction

Seismic anisotropy is the characteristic that seismic wave velocity varies with propagation direction, providing essential structural constraints on geodynamic evolution of the Earth. For example, crustal and upper mantle deformation often leads to seismic anisotropy, either due to lattice preferred orientation of anisotropic constituent minerals, or caused by shaped preferred orientation of isotropic materials with distinct shapes (Crampin & Booth, 1985; Long & Becker, 2010; Montagner & Guillot, 2002; Nicolas & Christensen, 1987; Silver, 1996). Different measurements have been proposed to reveal anisotropic structure such as shear wave splitting (Li et al., 2011; Savage, 1999), surface wave tomography (Russell et al., 2019; Yao et al., 2010), body wave tomography (Creasy et al., 2019; Zhao et al., 2016) and receiver functions (Schulte-Pelkum & Mahan, 2014; Zheng et al., 2021). Recovering seismic anisotropy using seismic tomography has key implications for understanding the dynamic processes of tectonic units.

In contrast to other methods, surface wave tomography has better vertical resolution of seismic anisotropy, making it a critical tool for measuring anisotropy in the crust and upper mantle (Becker et al., 2012; Ekström, 2011; Simons et al., 2002). In case of sufficient azimuthal path coverage, phase velocity and azimuthal anisotropy can be derived either from earthquake data (Montagner, 1986; Romanowicz, 2002; Yao et al., 2010) or ambient noise cross-correlations (Ritzwoller et al., 2011; Wapenaar et al., 2010). Compared with earthquake-based surface wave tomography, ambient noise tomography enables substantial additional coverage at short periods

Software: Yunpeng Chen
Supervision: Sjoerd A. L. de Ridder, Sebastian Rost, Zhen Guo, Yongshun Chen
Visualization: Yunpeng Chen, Xiaoyang Wu
Writing – original draft: Yunpeng Chen
Writing – review & editing: Yunpeng Chen, Sjoerd A. L. de Ridder, Sebastian Rost, Zhen Guo, Yongshun Chen

(Shapiro et al., 2005). Numerous array-based tomographic methods have been developed to derive anisotropy from ambient noise, such as eikonal and Helmholtz tomography (Lin et al., 2009; Lin & Ritzwoller, 2011), wave gradiometry (Cao et al., 2020; De Ridder & Curtis, 2017) and beamforming (Soergel et al., 2023; Wu et al., 2023).

Eikonal tomography is a surface wave tomography method that relates phase front tracking to local propagation direction dependent wave speed (Lin et al., 2009). Conventional eikonal tomography estimates azimuthal anisotropy by fitting a parametric function to phase velocities from different azimuths, obtained using an isotropic eikonal equation. De Ridder et al. (2015) proposed an elliptical-anisotropic eikonal tomography which employs ellipse parameters to characterize anisotropic velocity structures with an anisotropic eikonal equation. This method enables explicit regularization of the medium parameters and retrieves azimuthal anisotropic velocity robustly (De Ridder et al., 2015). However, the interpolation schemes in these eikonal tomography methods reduce the resolution since it smooths the phase traveltime surfaces beyond the level of the inter-station spacing.

In recent years, deep learning has been applied to diverse aspects of geoscience, such as geology (Ho et al., 2023; Kim & Yun, 2021), geomorphology (Li et al., 2020), geochemistry (Luo et al., 2020) and geophysics (Yang & Ma, 2019). Particularly, a broad range of methods using deep neural networks (DNNs) in seismology are proposed to leverage the increasing amount of observed data for modeling, prediction, detection and classification (Yu & Ma, 2021). These applications of utilizing deep learning to solve seismic problems include but are not limited to arrival time picking (Ross et al., 2018), seismic data processing (Zhu et al., 2019), earthquake location (Mousavi et al., 2020) and seismic imaging (Araya-Polo et al., 2018). As a data-driven method, classical DNNs have been proven to overcome some limitations in traditional seismic methods. But in these applications, the training data often imply some prior knowledge that is ignored in classical deep learning methods. This purely data-driven training is more susceptible to observation errors and leads to poor generalization of predicting seismic wave propagation outside of the span of the training data. Combining data-driven and physics-based models is a promising way for seismic machine learning.

Physics-informed neural networks (PINNs), a new kind of deep learning framework, were proposed by Raissi et al. (2019) to solve forward and inverse problems of partial differential equations (PDEs). PINNs utilize the capability of automatic differentiation which is widely used in training DNN and it also allows adding underlying physical laws to the loss function to combine the data-based model and theory-based model during the training process (Baydin et al., 2018; Karpatne et al., 2017). PINNs have gradually become a research highlight of scientific machine learning within various fields, such as fluid mechanics (Raissi et al., 2020), material science (Fang & Zhan, 2019), biomedicine (Kissas et al., 2020) and power systems (Misyris et al., 2020). During these applications, PINNs can train accurate and generalized models even with limited data by automatically incorporating physics constraints of the system.

Significantly, PINNs have already shown great potential in seismological applications. For forward problems, PINNs have been applied to the eikonal equation for traveltime calculation in isotropic and anisotropic media (Smith et al., 2020; Taufik et al., 2022; Waheed, Alkhalifah, et al., 2021; Waheed et al., 2020; Waheed, Haghighat, et al., 2021) and directly simulate wave equation solutions for acoustic and elastic wave propagation (Alkhalifah et al., 2020; Karimpouli & Tahmasebi, 2020; Moseley, Markham, & Nissen-Meyer, 2020; Moseley, Nissen-Meyer, & Markham, 2020; Song & Wang, 2023; Song et al., 2021, 2022). For inverse problems, PINNs have been proposed for exploration-scale seismic tomography with the factored eikonal equation (Gou et al., 2022; Waheed, Alkhalifah, et al., 2021; Waheed, Haghighat, et al., 2021) and wavefield reconstruction inversion (Song & Alkhalifah, 2021). A PINN algorithm has also been developed for full waveform inversion, as demonstrated through various synthetic case studies (Rasht-Behesht et al., 2022). Recently, Chen et al. (2022) presented the first application of PINNs to field seismic data for eikonal tomography, demonstrating their feasibility on real data sets and at scale. However, PINN-based tomography methods, especially for anisotropic models of field data, remains an open area for continued progress.

Here we propose a PINN based elliptical-anisotropy eikonal tomography (pinnEAET) to retrieve Rayleigh wave phase velocity and azimuthal anisotropy for multiple frequencies simultaneously. Two kinds of neural networks (NNs) are used to represent azimuthal dependence of phase velocities related matrices and phase traveltime surfaces (Figure 1). We apply our algorithm to field data gained from a dense network of stations on the northeastern Tibetan Plateau and discuss the advantages and challenges of the proposed approach.
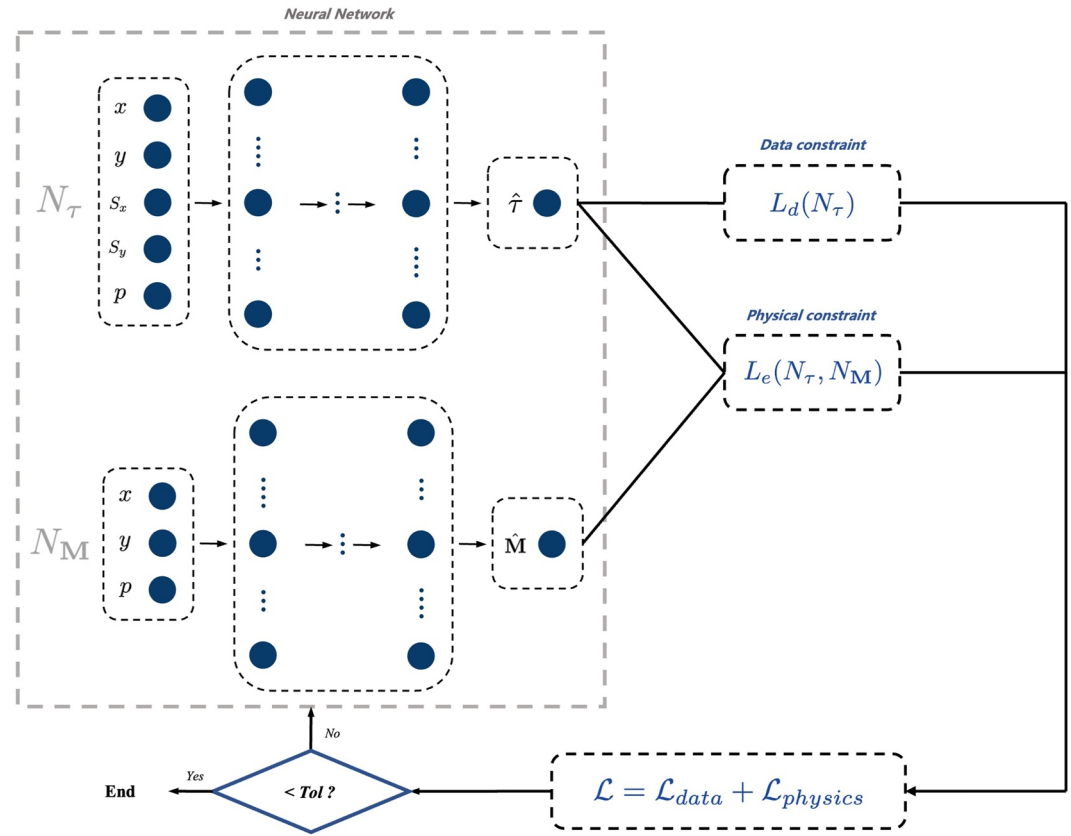
Figure 1. Schematic of PINN framework for elliptical-anisotropic eikonal tomography, where N_τ and N_M are the traveltime and medium property NNs, x, y and s_x, s_y are spatial location coordinates of receivers and sources respectively, p contains discrete distinct periods for the multi-period solutions, $\hat{\tau}$ and $\hat{M}$ are the outputs of trained traveltime and medium properties, $L_d(N_\tau)$ represents the observed Rayleigh wave traveltime data constraint, $L_e(N_\tau, N_M)$ represents the elliptical-anisotropic eikonal equation constraint. The neural network part on the left is used to approximate the solution, while the data and physics constraints part on the right is used to optimize the network parameters. The training process ends when the loss function $\mathcal{L}$ is less than a given tolerance.

2. Methods

In this section, we will introduce the fundamental aspects of elliptical-anisotropic eikonal equation, then describe incorporating this PDE into a PINN framework, and finally share the idea of estimating the Rayleigh wave anisotropic phase velocity from the trained networks.

2.1. Elliptical-Anisotropic Eikonal Equation

In the wave number domain, the phase velocity $c = c(\phi, \boldsymbol{x}, \omega)$ at location $\boldsymbol{x} = (x, y)$ and frequency ω, where ϕ is the direction of wave propagation, exhibiting elliptical-anisotropic azimuthal anisotropy can be defined as (De Ridder et al., 2015):

$$c^2(\phi) = c_f^2 \cos^2(\phi - \alpha) + c_s^2 \sin^2(\phi - \alpha), \tag{1}$$

where $c_f = c_f(\boldsymbol{x}, \omega)$ and $c_s = c_s(\boldsymbol{x}, \omega)$ are the fast and slow velocities, respectively. $\alpha = \alpha(\boldsymbol{x}, \omega)$ is the azimuth of the fast direction. Equation 1 describes an ellipse with the major and minor radii corresponding to c_f and c_s.

To derive an eikonal equation for elliptical anisotropy, the scalar wavefield is transformed from the wave number domain to the spatial domain and the phase traveltime $\tau = \tau(\boldsymbol{x}, \boldsymbol{x}_s, \omega)$ for a given source location $\boldsymbol{x}_s = (x_s, y_s)$ at a specific frequency ω (also known as the linear phase) is introduced (Aki & Richards, 2002).

In the high-frequency approximation, we can find the elliptical-anisotropic eikonal equation (De Ridder et al., 2015):

$$1 = \begin{bmatrix} \partial_x \tau & \partial_y \tau \end{bmatrix} \begin{bmatrix} M_{11} & M_{12} \\ M_{21} & M_{22} \end{bmatrix} \begin{bmatrix} \partial_x \tau \\ \partial_y \tau \end{bmatrix}. \tag{2}$$

The matrix elements are respectively expressed as:

$$M_{11} = M_{11}(\boldsymbol{x}, \omega) = \left(c_f^2 - c_s^2\right)\sin^2(\alpha) + c_s^2, \tag{3}$$

$$M_{12} = M_{21} = M_{12}(\boldsymbol{x}, \omega) = \left(c_f^2 - c_s^2\right)\sin(\alpha)\cos(\alpha), \tag{4}$$

$$M_{22} = M_{22}(\boldsymbol{x}, \omega) = \left(c_f^2 - c_s^2\right)\cos^2(\alpha) + c_s^2. \tag{5}$$

Then the problem of solving the phase velocities and azimuthal anisotropy converts to computing the eigenvalues (c_f^2 and c_s^2, representing the fast and slow velocities) and eigenvectors (indicating the fast and slow directions) of the matrix $\boldsymbol{M} = \begin{bmatrix} M_{11} & M_{12} \\ M_{21} & M_{22} \end{bmatrix}$. For the 2×2 matrices $\boldsymbol{M}$, there is an explicit algebraic solution of the eigenvalues and eigenvectors. In this way, the fast and slow velocity can be computed as:

$$c_f = c_f(\boldsymbol{x}, \omega) = \sqrt{\frac{\left(M_{11} + M_{22} + \sqrt{(M_{11} + M_{22})^2 - 4\left(M_{11}M_{22} - M_{12}^2\right)}\right)}{2}}, \tag{6}$$

$$c_s = c_s(\boldsymbol{x}, \omega) = \sqrt{\frac{\left(M_{11} + M_{22} - \sqrt{(M_{11} + M_{22})^2 - 4\left(M_{11}M_{22} - M_{12}^2\right)}\right)}{2}}, \tag{7}$$

and if M_{12} is not zero, the fast direction of anisotropy can be defined as:

$$\alpha(\boldsymbol{x}, \omega) = \arctan\left(\frac{c_f - M_{22}}{M_{12}}\right). \tag{8}$$

Note that this is just one specific way to represent the fast and slow velocity and the azimuthal angle. Consequently, the isotropic component, which is the radius of a circle with an area equal to the velocity ellipse (Weisstein, 2014), can be calculated as:

$$c_0 = c_0(\boldsymbol{x}, \omega) = \sqrt{c_f c_s}. \tag{9}$$

Alternatively, we could have used the average between the fast and slow velocity $c_0 = (c_f + c_s)/2$. The anisotropic component can be characterized as either eccentricity, $e = e(\boldsymbol{x}, \omega) = \sqrt{1 - \frac{c_s^2}{c_f^2}}$, flattening factor, $f = f(\boldsymbol{x}, \omega) = 1 - \frac{c_s}{c_f}$ (Weisstein, 2014), or equivalent amplitude (Smith & Dahlen, 1973):

$$A = A(\boldsymbol{x}, \omega) = \frac{c_f - c_s}{2} \tag{10}$$

Here we use equivalent amplitude A to represent the strength of anisotropy commonly used in other studies (Hao et al., 2021; Kästle et al., 2022; Lin et al., 2009).

2.2. Elliptical-Anisotropic Eikonal Tomography Using PINNs

In order to approach this problem, we first consider a feed-forward NN (see Figure 1), which consists of L layers with network parameters $\boldsymbol{W}$ and $\boldsymbol{b}$:

$$\boldsymbol{z}^l = \sigma\left(\boldsymbol{W}^l \cdot \boldsymbol{z}^{l-1} + \boldsymbol{b}^l\right), \quad l = 1, \ldots, L, \tag{11}$$

where L is the maximum number of layers with l being the layer. z refers to the affine transformations between the layers of NN, when $l = 1$, z^0 represents inputs of the model; when $l = L$, $z^L = N(\boldsymbol{W}^1, \ldots, \boldsymbol{W}^L, \boldsymbol{b}^1, \ldots, \boldsymbol{b}^L; z^0)$, where N is the NN, represents the outputs of the model and other z^l, $l = 2, \ldots, L - 1$ represent the neurons in hidden layers. σ is the activation function that is usually nonlinear. $\boldsymbol{W}^l$ and b^l are the weights and the biases of each layer l, respectively. Training a feed-forward NN involves passing data through interconnected layers that learn to map features in a hierarchical fashion, with backward-propagated weight adjustments.

We take the traveltime $\tau = \tau(\boldsymbol{x}_r, \boldsymbol{x}_s, \omega)$, where $\boldsymbol{x}_r, \boldsymbol{x}_s$ are receiver and source locations, as the field value of the NN architecture. Whereas the trainable parameters ($\boldsymbol{W}$ and $\boldsymbol{b}$) are represented with θ, the chosen parameters such as number of layers, neurons and type of activation functions are unique for each NN and denoted with the subscript to N. Then a transformation of Equation 11 can be used to represent an approximate solution for phase traveltime surfaces $\tau = \tau(\boldsymbol{x}, \boldsymbol{x}_s, \omega)$ in the eikonal equation:

$$\tau(\boldsymbol{x}, \boldsymbol{x}_s, \omega) = N_\tau(\theta_\tau; \boldsymbol{x}, \boldsymbol{x}_s, \omega) = N_\tau\left(\boldsymbol{W}^1, \ldots, \boldsymbol{W}^L, \boldsymbol{b}^1, \ldots, \boldsymbol{b}^L; z^0\right) \tag{12}$$

where θ_τ indicates the trainable parameters of the traveltime NN, N_τ. In this case, the inputs in Equation 11 are $z^0 = (\boldsymbol{x}_r, \boldsymbol{x}_s, \omega)$ for specific coordinates and the outputs are $z^L = (\boldsymbol{x}, \boldsymbol{x}_s, \omega)$ for generic coordinates. The main idea of training the NN is to find the appropriate weights and biases to minimize the errors between the observations and predictions, where the sum of errors defines the loss function. For a specific frequency ω, we use the mean squared error (MSE) with an L2 norm to define the loss function only including a difference between predictions and observations:

$$\mathcal{L}_d(\theta_\tau) = \sum_j^{N_{src}} \sum_i^{N_{rcv}} \left| N_\tau(\theta_\tau; \boldsymbol{x}_{r;i}, \boldsymbol{x}_{s;j}, \omega) - \tau_{i,j} \right|^2, \tag{13}$$

where $\mathcal{L}_d$ is the loss function of the data constraint, i and j are the index of receivers and sources, respectively, N_{src} is the number of sources, N_{rcv} is the number of receivers, $\boldsymbol{x}_{r;i} = (x_r, y_r)_i$ and $\boldsymbol{x}_{s;j} = (x_s, y_s)_j$ are the receiver and source locations, $\tau_{i,j}$ represents the observed traveltime data.

In classical NN architecture, the phase traveltime surfaces of seismic waves are denoted as in Equation 13. This data-constrained loss can learn features based on observed data but has no knowledge of the underlying physical principles. Unlike this purely data dependent training, PINNs enable NNs to naturally meet the physical laws by modifying the loss function and modulating the training phase. In this study, the PINN framework is realized in SciAnn, a Keras and Tensorflow wrapper designed with physics-informed deep learning (Haghighat & Juanes, 2021). Our model incorporates Equation 2 to govern the Rayleigh wave propagation, and the physics-constrained loss function at a single frequency can be written as:

$$L_e(N_\tau, N_{\boldsymbol{M}}) = N_{M11}\partial_x^2 N_\tau + 2N_{M12}\partial_x\partial_y N_\tau + N_{M22}\partial_y^2 N_\tau - 1, \tag{14}$$

where L_e is the loss function of the elliptical-anisotropic eikonal constraint, $N_{\boldsymbol{M}} = N_{\boldsymbol{M}}(\theta_{\boldsymbol{M}}; \boldsymbol{x}_r, \omega) = [N_{M11}(\theta_{M11}; \boldsymbol{x}_r, \omega), N_{M12}(\theta_{M12}; \boldsymbol{x}_r, \omega), N_{M22}(\theta_{M22}; \boldsymbol{x}_r, \omega)]$ specify the NNs of medium property matrices $\boldsymbol{M}$ in Equation 2, $N_\tau = N_\tau(\theta_\tau; \boldsymbol{x}_r, \boldsymbol{x}_s, \omega)$ is the traveltime at $\boldsymbol{x}_r$ from the source location $\boldsymbol{x}_s$. θ_τ and $\theta_{\boldsymbol{M}}$ indicate parameters of traveltime NN, N_τ and medium property NNs, $N_{\boldsymbol{M}}$, respectively. Please note that here we use three NNs to represent the medium property matrices described by Equations 3–5, but they share the same NN parameters. To enhance the robustness and efficiency of our methodology, we also explore the use of a single medium property NN for representing the three medium property matrices (M_{11}, M_{12}, M_{22}). Our findings reveal that although a single large network led to a reduction in training time, it also introduced unexpected artifacts, particularly noticeable at the corners of velocity maps (Figure S3 in Supporting Information S1). These artifacts are likely due to the lower sampling at the edge of our study areas. Detailed results and further discussion can be found in the Supporting Information S1.

Equations 13 and 14 demonstrate single frequency loss functions. In practice, surface waves at different frequencies have depth-dependent sensitivity expressed as sensitivity kernels. So multi-frequency solutions are required for Rayleigh wave tomography to fully resolve the medium. Here we extend the NNs of the traveltime and medium property matrix to contain a period term as input so that the results of different periods can be obtained

by training the network only once. For the case of simultaneous optimization of anisotropic velocities at k frequencies, the multi-frequency total loss function that consists of data and physics constraints is expressed as:

$$
\mathcal{L}(\theta_\tau, \theta_{\boldsymbol{M}}) = \sum_{k}^{N_{freq}} \sum_{j}^{N_{src}} \sum_{i}^{N_{rcv}} \left[\left| N_\tau(\theta_\tau; \boldsymbol{x}_{r;i}, \boldsymbol{x}_{s;j}, \omega_k) - \tau_{i,j,k} \right|^2 \right.
$$
$$
\left. + \epsilon_e \left| L_e(N_\tau(\theta_\tau; \boldsymbol{x}_{r;i}, \boldsymbol{x}_{s;j}, \omega_k), N_{\boldsymbol{M}}(\theta_{\boldsymbol{M}}; \boldsymbol{x}_{r;i}, \omega_k)) \right|^2 \right],
\tag{15}
$$

where k and N_{freq} are the frequency index and maximum number of frequencies, ω_k represents the selected frequency k, $\tau_{i,j,k}$ is the phase traveltime surface at frequency k. ϵ_e is a weight factor set to normalize the different terms of data and physics constraints. The value of ϵ_e has been determined through synthetic tests and can be chosen within a narrow range: large enough to allow velocity model updates but small enough to enforce the physics constraints. The collocation points to evaluate the physics constraints coincide with the available data locations, although other choices are possible. In this network, the inputs are the spatial coordinates of observed source and receiver locations and given period values. For displaying purposes, the trained NNs are evaluated on a chosen set of points forming a grid over a chosen extent. The network must be designed to have sufficient capability to represent the diversity and complexity in a set of phase traveltime surfaces over anisotropic velocity structures. By including physics constraints as loss terms, pinnEAET is fundamentally a joint state and parameter space approach.

The objective of the elliptical-anisotropy eikonal tomography is to estimate velocity structure and azimuthal anisotropy. The fast and slow velocity and the azimuth information can be directly evaluated from the trained networks $N_{\boldsymbol{M}}$. Meanwhile, the reconstructed phase traveltime surfaces $\hat{\tau}$ can be obtained by training the networks N_τ. With the loss term of elliptical-anisotropic eikonal equation, these trained phase traveltime surfaces can capture the constrained velocity information by calculating their gradients. The updated network parameters are generated by minimizing the MSE loss function:

$$
\arg\min_{\theta_\tau, \theta_{\boldsymbol{M}}} \{ \mathcal{L}(\theta_\tau, \theta_{\boldsymbol{M}}) \} \rightarrow \hat{\theta}_\tau, \hat{\theta}_{\boldsymbol{M}}.
\tag{16}
$$

where $\hat{\theta}_\tau$ specifies the parameters of the trained network N_τ while $\hat{\theta}_{\boldsymbol{M}}$ specifies the parameters of the trained network $N_{\boldsymbol{M}}$.

Once the networks are trained based on the observed data points, we can directly evaluate the phase traveltime surfaces and three medium property matrices (Equations 3–5) at regular sampling grid points. The final Rayleigh wave phase velocity solution can be extracted in two ways based on the trained networks. One way is to solve the eigenvalue and eigenvector problem of the inverted medium properties. The inverted Rayleigh wave phase velocity is shown in Equation 9. The orientation of the anisotropic fast axes and the magnitude of anisotropy can be computed as Equations 8 and 10. Employing this method we can directly obtain the isotropic phase velocity and anisotropic amplitude and directions. An alternative way to extract the velocity information from the trained networks is to calculate the gradient of the trained phase traveltime surfaces:

$$
\bar{c}(\boldsymbol{x}, \omega) = \frac{1}{N_{src}} \sum_{j}^{N_{src}} \frac{1}{\left| \nabla N_\tau(\hat{\theta}_\tau; \boldsymbol{x}, \boldsymbol{x}_{s;j}, \omega_k) \right|},
\tag{17}
$$

where $\bar{c}$ is the average velocity surface from all predicted phase traveltime surfaces, N_τ indicates the trained phase traveltime surfaces $\hat{\tau}$. In order to reduce or even eliminate the influence of singular values near the sources, we take a trimmed geometric mean to exclude the 10 percentile outliers of the traveltime gradient data sets (Chen et al., 2022). We also calculate the associated standard deviation between the phase velocities from individual virtual sources and the average phase velocity $\bar{c}$ at each frequency and spatial location. This process results in phase velocity standard deviations at each location, providing estimates of standard uncertainties in our model. Both Equations 9 and 17 can illustrate the isotropic phase velocity of Rayleigh waves and their results are quite similar. Given that gradient calculations may introduce errors, here we choose Equations 8–10 as isotropic and anisotropic components. The trained phase traveltime surfaces $\hat{\tau}$ and average phase velocities in Equation 17 are used to measure the uncertainties.
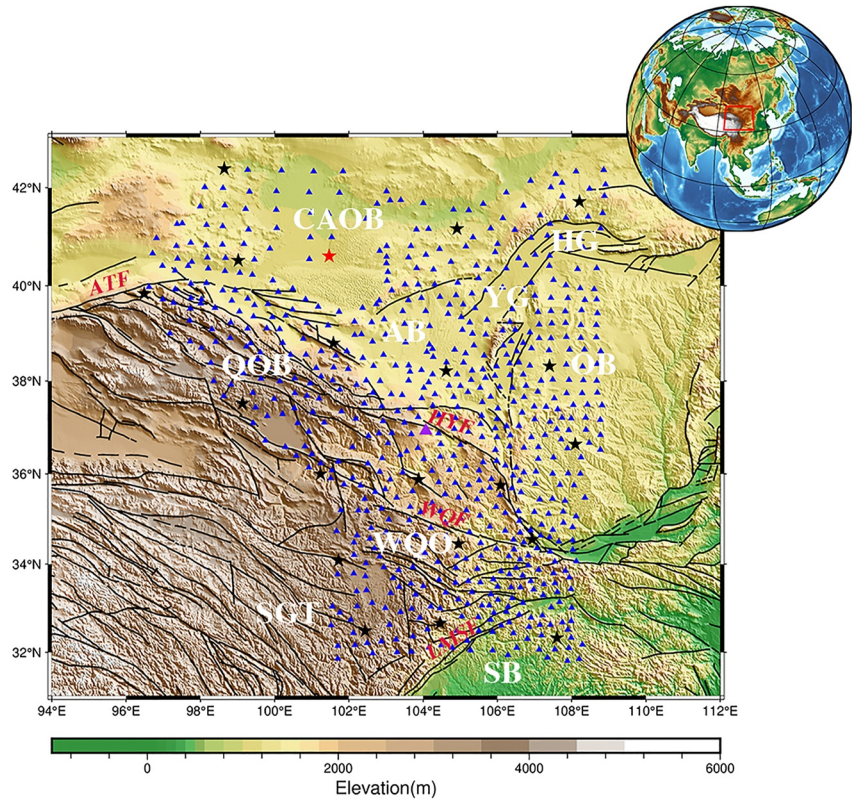
Figure 2. Dense seismic array geometry deployed on the northeastern Tibetan Plateau. Black lines indicate the main faults, blue triangles indicate stations from ChinArray-Himalaya II and stars indicate the selected source stations used in this study. The main faults and tectonic blocks are labeled as: ATF = Altyn-Tagh Fault; HYF = Haiyuan Fault; LMSF = Longmenshan Fault; WQF = West-Qinling Fault; AB = Alxa Block; CAOB = Central Asian Orogenic Belt; HTB = Hetao Graben; OB = Ordos Block; QOB = Qilian Orogenic Belt; SB = Sichuan Basin; SGT = Songpan-Ganzi Terrane; WQO = Western Qinling Orogen; YCG = Yinchuan Graben.

3. Results

3.1. Training Data

In this section, we apply our algorithm to ambient noise cross-correlation multi-frequency Rayleigh wave phase traveltime data recorded by the dense seismic array ChinArray-Himalaya II (Figure 2). Since 50 Ma, the continuous collision of India and Eurasia continents has led to high topography and crustal thickening within the Tibetan Plateau interior that primarily affects the tectonics in Asia (Molnar & Tapponnier, 1975; Yin & Harrison, 2000). The northeastern Tibetan Plateau plays a key role in studying the geodynamic mechanism of the crustal thickening and deformation of the Tibetan Plateau. Several hypotheses for the topographic elevation have been proposed (e.g., crustal flow (Clark & Royden, 2000; Royden et al., 1997); oblique subduction of lithospheric mantle and strike-slip extrusion (Tapponnier et al., 2001); thin viscous sheet model (England & Houseman, 1986)) to explain the mechanism of continental deformation, but the precise source of deformation remains enigmatic and subject to debate.

For the ChinArray-Himalaya II array, a total of 676 stations were deployed between 2013 and 2016 for about 2.5 years of continuous recordings with a station spacing of 40–70 km. Due to the good coverage of the northeastern Tibetan Plateau, these data enable us to test the capability of the proposed approach. In addition, the ChinArray-Himalaya II data set has also been used to study the Rayleigh wave phase velocity and anisotropy using various methods, for example, two-station Rayleigh wave tomography (Li et al., 2017), joint receiver functions and Rayleigh wave tomography (Wang et al., 2017), beamforming Rayleigh wave tomography (Wang et al., 2020) and Rayleigh wave eikonal tomography (Hao et al., 2021). These results enable comparison of the performance of the pinnEAET approach.
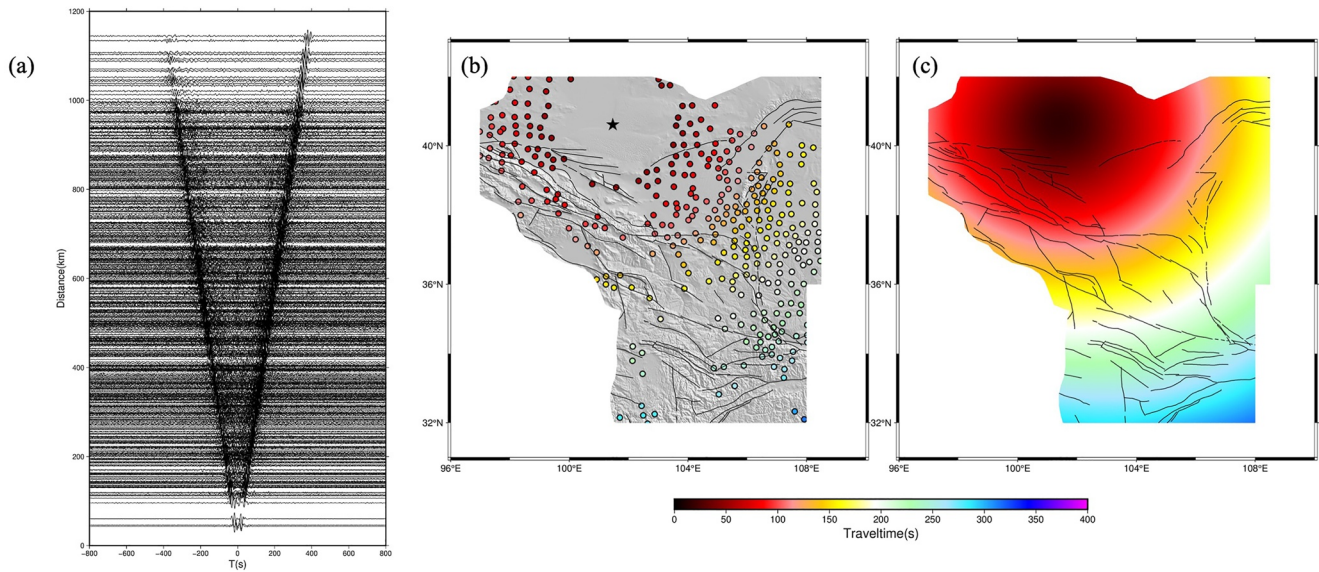
Figure 3. (a) The stacked waveform of Z-Z component cross-correlations for station pairs at station WT045 (red star in Figure 2) for a period range of 10–40 s, the V-shaped arrivals indicate the signals of Rayleigh wave; (b) The 25 s Rayleigh wave phase traveltime measured from cross-correlation centered on station WT045 shown as a star; (c) The 25 s Rayleigh wave phase traveltime surfaces predicted at station WT045 using pinnEAET.

The training phase traveltime data are generated following the seismic ambient noise data processing steps as in Bensen et al. (2007) and Lin et al. (2008): the Z component of raw data are processed by resampling, removing the instrument response, filtering and applying temporal and spectral normalization. Traveltime calculation involves cross-correlating signals across station pairs and measuring the phase delay (or traveltime) of the resulting waveform. Figure 3a shows an example of Z-Z component cross-correlations for station pairs associated with station WT045, filtered in the period range 10–40 s. Under ideal conditions, ambient noise cross-correlations should yield empirical Green's functions in both causal and anti-causal time windows (Lobkis & Weaver, 2001; Wapenaar, 2004). In Figure 3a, the energy of the fundamental Rayleigh wave can be clearly captured for both causal and anti-causal time windows. Figure 3b shows the measured Rayleigh wave phase traveltime data centered on station WT045 at 25 s period. After picking phase traveltimes, 20 source stations are quasi-randomly selected among all 676 stations to achieve good coverage of the geographic area (Figure S1 in Supporting Information S1). The training targets are determined by the selected 20 phase traveltime surfaces. Figure 3c shows an example of the 25 s Rayleigh wave phase traveltime surface evaluated from the trained N_τ at the effective source station WT045. It is worth emphasizing that receivers located within two wavelengths radius of each source are removed, because traveltime measurements collected at distances shorter than 1–2 wavelengths are unreliable (Lin et al., 2009).

3.2. Resolution Tests

Before applying our approach to field data, we perform checkerboard tests to assess the performance of the pinnE-AET and tune the NN design. As shown in Figures 4a–4d, the isotropic synthetic checkerboard model assumes a constant background velocity defined by subtracting the observed frequency-dependent traveltime from the inter-station distances. Then ±2% of alternating velocity perturbations are added to the initial model to build the synthetic phase velocity model for checkerboard tests. There are 8 × 8 anomalies at each period with a maximum radius of 75 km for each anomaly. These alternating low and high velocity patterns are distributed at 150 km intervals in latitude and longitude direction, respectively. The network parameters used in the checkerboard tests are consistent with the parameters of the subsequent field data training. The synthetic traveltimes of the checkerboard model are calculated using the fast marching method based on the eikonal equation (Sethian, 1999; Treister & Haber, 2016), and 0.1 s Gaussian random noise with a standard deviation of 0.01 is added to the synthetic traveltime data to simulate the noise level in observed data.

Figures 4e–4h shows the cross-section view of the retrieved Rayleigh wave phase velocity maps at 10, 20, 30, and 40 s for the resolution tests. It can be seen that the inversion recovers the pattern of velocity variation well. The resolution of less sampled structures at the periphery of the station network is still satisfactory. The northern part
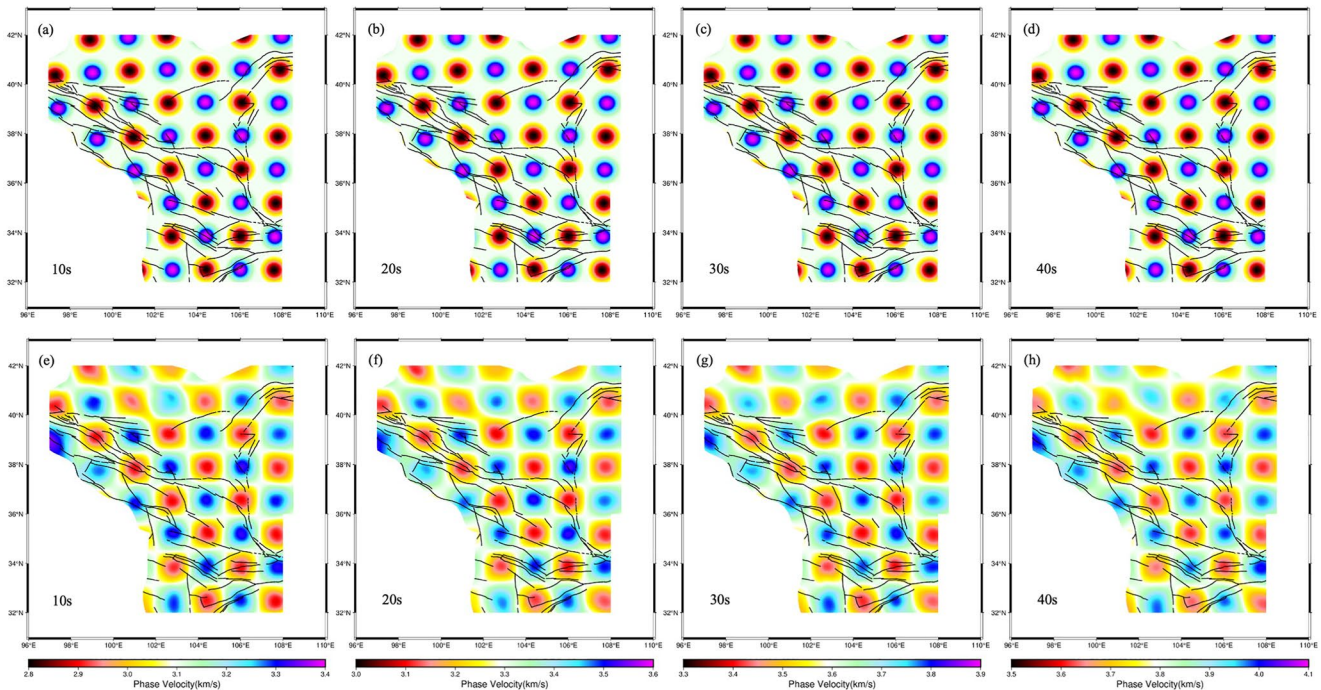
Figure 4. (a–d) Input synthetic Rayleigh wave phase velocity model of checkerboard resolution tests at periods of 10, 20, 30, and 40 s; (e–h) Corresponding retrieved velocity slices using pinnEAET.

of the network exhibits lateral blurring in the SW-NE direction and the edges of the velocity anomalies appear indistinct. These may be linked to the selection of the source distribution.

3.3. Phase Velocities and Azimuth Anisotropy Beneath Northeastern Tibetan Plateau

As discussed in the Methods section, the pinnEAET algorithm consists of two different structures of networks (see Figure 1) with a total of four fully connected feed-forward NNs: one traveltime NN N_τ and three medium property NNs N_M. In addition to a parameter of target period k, N_τ training requires spatial locations and corresponding observed traveltimes, whereas N_M needs only spatial coordinates. Both networks are set to have 20 hidden layers. There are 80 neurons in each layer for N_τ while we use 60 neurons for all N_M. The number of neurons and hidden layers in the NNs were chosen based on the checkerboard tests and adjusted to accurately represent all phase traveltime surfaces, without compromising the uncertainty in the final anisotropic velocity and azimuthal anisotropy. The network was trained using an Adam optimizer over 5000 epochs (Kingma & Ba, 2014), with a learning rate of 0.001. These training parameters were chosen based on systematic synthetic tests for accurately and efficiently extracting maximum details from field data. Figure 5 shows the convergence processes of three loss functions: data constraints, physics constraints as well as total loss. These terms converge quickly and uniformly to below 10^{-3}, indicating that the model has a fast learning speed and the training process exhibits strong stability.
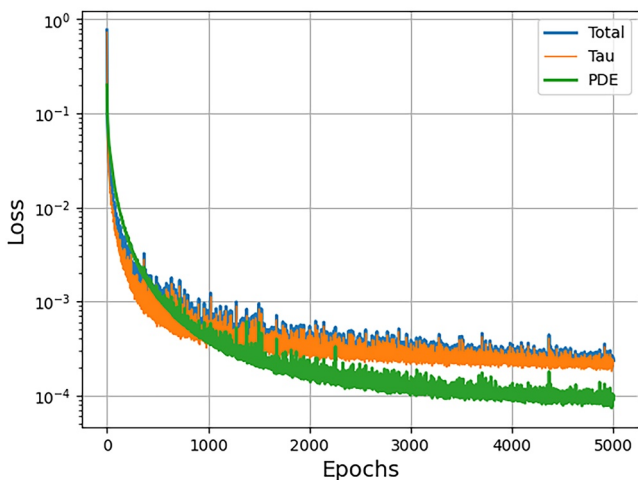
Figure 5. History of convergence of the total loss function (Total), the data constraint (Tau) and physics constraint (PDE) in Equation 15 for pinnEAET in the northeastern Tibet.

The results of analyzing Rayleigh wave phase velocity and azimuthal anisotropy over periods of 10, 20, 30, and 40 s in northeastern Tibet are shown in Figure 6. Figure 7 shows the corresponding uncertainties estimated from the traveltime NNs (Equation 17). The uncertainties for all periods are below 50 m/s and below 20 m/s in most areas. Compared to the central study area, the uncertainties tend to be higher along the boundaries. The higher uncertainty in the Hetao Graben at 10 s is likely due to the lower signal-to-noise
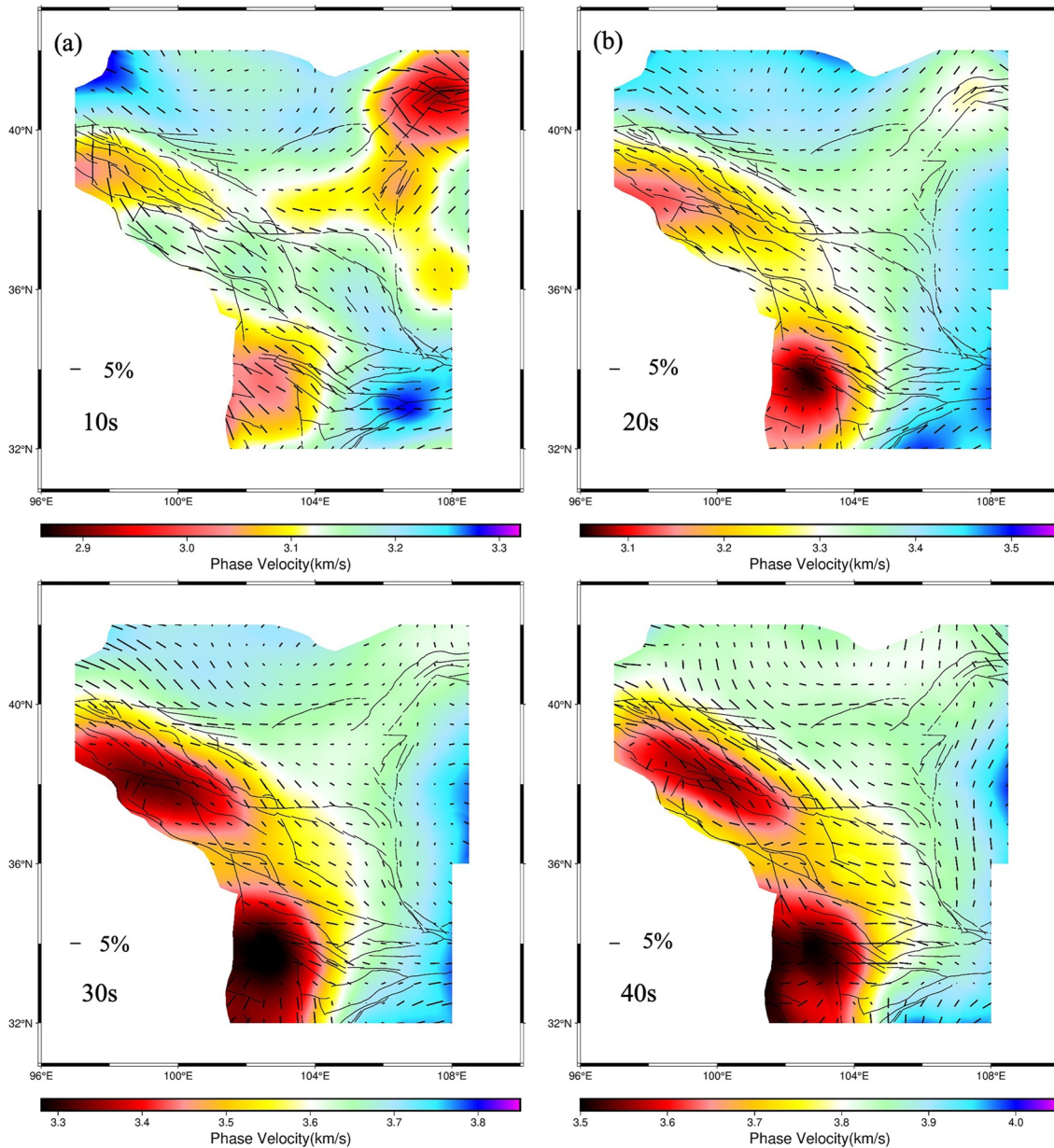
Figure 6. (a–d) Azimuthal anisotropic phase velocity at periods of 10, 20, 30, and 40 s beneath northeastern Tibetan Plateau using pinnEAET. Black bold vectors indicate the strength and fast propagation direction of anisotropy, black thin lines indicate main faults.

ratio at shorter periods in that region. Although the uncertainties increase slightly with period, the overall reliability remains high.

For azimuthally dependent phase velocity, as a whole the distribution of low or high velocity zones and anisotropic fast directions seem significantly controlled by the fault strikes and block boundaries. Prominent low velocity zones (LVZs) exist at almost all periods along the southwestern boundary of the study area, corresponding to the Qilian Orogenic Belt and the Songpan-Ganzi Terrane, and relatively high velocities appear in the northern and southeastern regions, corresponding to the Central Asian Orogenic Belt, Western Qinling Orogen and Sichuan Basin. The fast directions of azimuthal anisotropy changes slowly at each period.
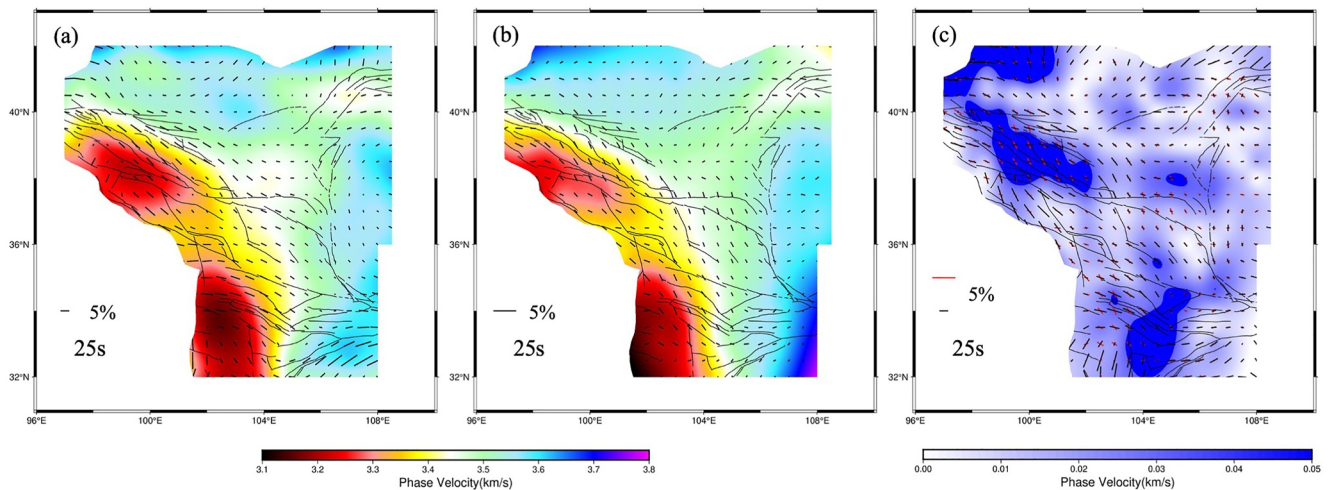
The 10 s azimuthal anisotropic phase velocity is sensitive to the structure of the shallow sedimentary layer and the upper crust. Unlike other periods, it is primarily distinguished by the presence of LVZs in the northeast and relatively high velocity zone (HVZ) in the southeast of the study area. These LVZs are closely associated with the
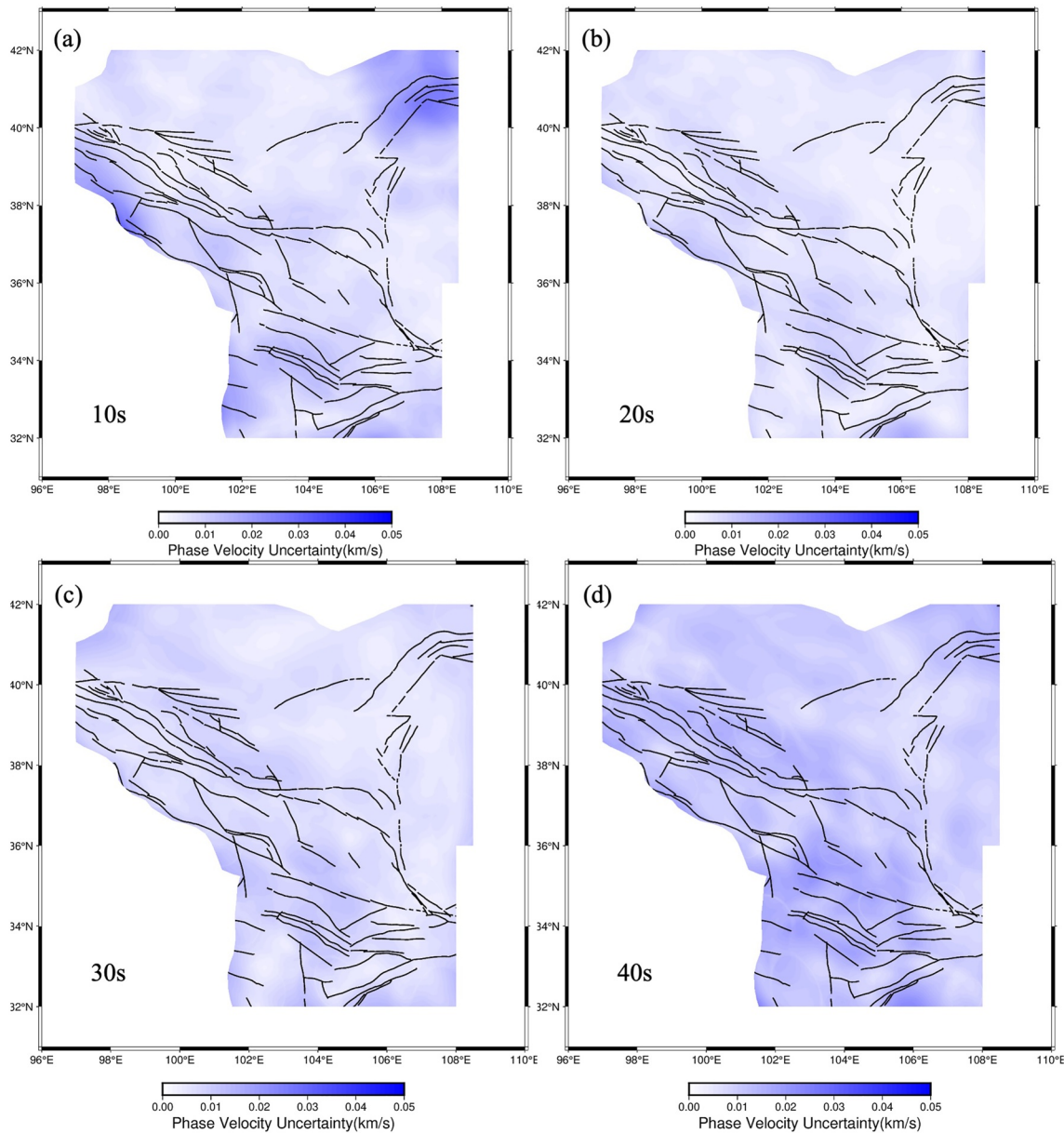
Figure 7. (a–d) Uncertainty map of the Rayleigh wave phase velocity at periods of 10, 20, 30, and 40 s beneath northeastern Tibetan Plateau using pinnEAET.

sedimentary basins in Hetao Graben, Yinchuan Graben, Alxa Block and Ordos Block, while the relatively HVZ may be linked to the exposure of metamorphic rocks and granites in the east of the Western Qinling orogen and the northern Sichuan Basin (Wang et al., 2020). The anisotropic fast direction is related to fault strikes and block boundaries in most study areas. The fast direction in the southwest regions of Qilian Orogenic Belt, Western Qinling Orogen and Songpan-Ganzi Terrane is mainly in NE-SW direction. The fast directions at 10 s beneath the Songpan-Ganzi Terrane are not consistent with longer periods, supporting the idea that crustal flows are predominantly found in the middle and lower crust (Gao et al., 2020; Li et al., 2022).

The 20 s azimuthal anisotropic phase velocity mainly represents structures of the mid-crust. Relative to the velocity distribution at 10 s, the low velocity anomalies in Yinchuan Graben, Alxa block and Ordos Block disappear, but there is still a smaller LVZ in the Hetao Graben. The northwestern (Central Asian Orogenic Belt) and southeastern parts (Sichuan Basin) are characterized by relatively high velocity anomalies without clear boundaries. In the southwest corner of the study area the fast directions resolved by periods of 10 and 20 s are similar.

Figure 8. (a) The 25 s azimuthal anisotropic phase velocity beneath northeastern Tibetan Plateau using pinnEAET; (b) The 25 s azimuthal anisotropic phase velocity generated by conventional eikonal tomography; (c) The difference between 25 s azimuthal anisotropic phase velocity (background) from pinnEAET (black lines) and eikonal tomography (red lines).

It shows a tendency of near clockwise rotation along the margin of the northeastern Tibetan Plateau. The anisotropic strength is relatively weak in the Ordos Block.

The 30–40 s azimuthal anisotropic phase velocity illustrates the lower crustal and part of upper mantle structures. The main features in these periods are significant LVZs in the southwest and high velocity in the northeast. As the period increases, the velocity difference between the Tibetan Plateau and the surrounding areas progressively becomes more pronounced. The anisotropic strength increases noticeably in areas such as the Central Asian Orogenic Belt and Qilian Orogenic belt, which is possibly related to the inhomogeneity of the Moho (Zhang et al., 2020).

4. Discussion

Figure 8 shows a comparison of the azimuthal anisotropic velocities obtained by pinnEAET and traditional anisotropic eikonal tomography. We find very good agreement in the Rayleigh wave phase velocity structures in most regions with differences of under 50 m/s. Two major differences between the results exist in the northwest corner of the study area as well as part of the Qilian Orogenic Belt along the margin of the northeastern Tibetan Plateau where the result of conventional eikonal tomography shows significant high velocity zones that are not visible in other results. These could be spurious anomalies caused by less path coverage at the boundary. A similar discrepancy can be found in a small region in the center (105°E, 37°N) of the study area. To facilitate the analysis, we also compare the results of azimuthal double beamforming tomography (Wu et al., 2023) (Figure S2 in Supporting Information S1) and no differences of more than 50 m/s were found in these areas except for a very small area at the edge of the northeast corner, which also confirms the reliability of our method.

In the case of anisotropy, the pinnEAET directly calculates an equivalent amplitude of anisotropy using Equation 10 whereas traditional eikonal tomography fits a function of phase velocity variations over azimuth. Due to the different strategies, we only compare the azimuth of the fast propagation direction of those results. Both of them exhibit a trend of clockwise rotation in the fast direction along the margin of northeastern Tibetan Plateau. They show similar distribution of azimuthal anisotropy inside the study area, except that our anisotropic results illustrate the NWW-SEE-dominated fast direction in the Western Qinling Orogen rather than the NNW-SSE-dominated fast direction obtained by the conventional eikonal tomography. It is worth pointing out that our fast direction results have a better correspondence with the strikes of the West-Qinling Fault. In the center of the study area, south of the Alxa block, the fast directions of anisotropy of the two are not consistent, but our results are in good agreement with those of azimuthal double beamforming tomography (Figure S2c in Supporting Information S1). The anisotropy results for both differ considerably at the boundaries of the study area, especially in the northeast corner (Hetao Graben). Combined with Figure S2c in Supporting Information S1,
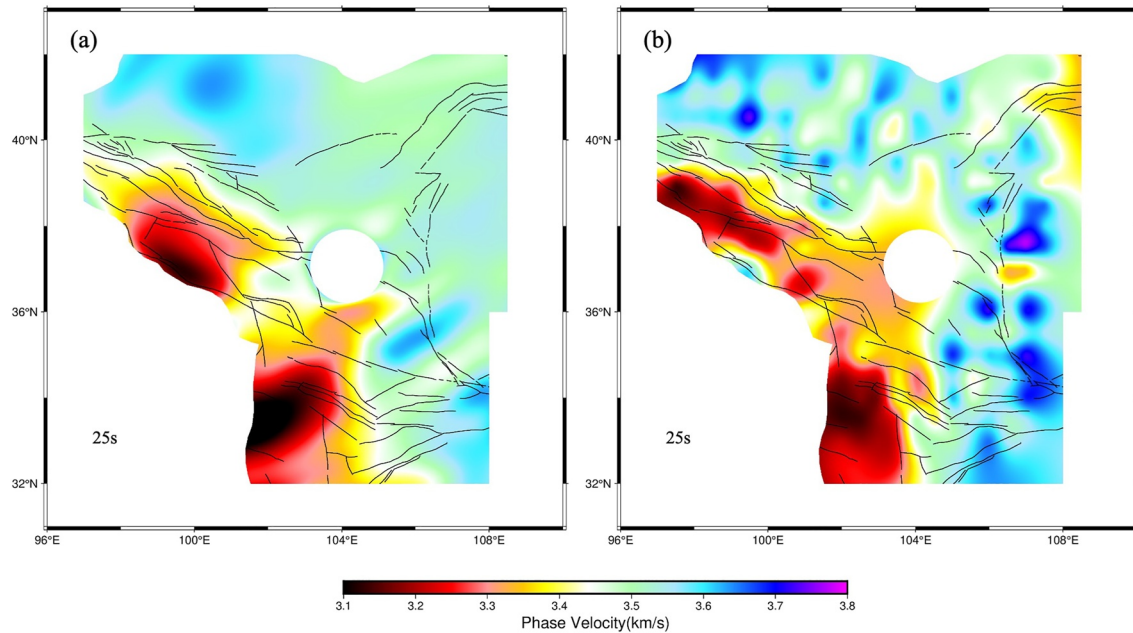
Figure 9. (a) The 25 s Rayleigh wave phase velocity beneath northeastern Tibetan Plateau using pinnEAET with only one source station (purple triangle in Figure 2); (b) The 25 s phase velocity generated by conventional eikonal tomography with same data sets.

the anisotropy results of all three methods differ in this region, which may be due to the fact that the path distribution on the boundary is relatively poor from some directions.

We also compare our anisotropic phase velocities with past studies in the region to assess the validity of the pinnEAET to the alternative approaches employed, such as teleseismic data based surface wave tomography (Hao et al., 2021; Li et al., 2017) and ambient noise beamforming tomography (Wang et al., 2020). These phase velocity results corroborate the velocity distribution of the southwest low velocities and northeast high velocities in the study area. The anisotropy results are also overall similar compared to those of Hao et al. (2021), only differing in small regions at certain periods. For example, for the 25 s period, our result shows a NW-SE fast direction in the northeast of Songpan-Ganzi Terrane (104°E, 33°N), while their result shows a near N-S direction. This is probably caused by the difference in the generation mechanism and information content between ambient noise data and teleseismic surface wave data. Combining the above comparisons, our results are consistent with those of other methods, confirming the viability of our pinnE-AET approach.

To verify the accuracy and reliability of the pinnEAET for small data sets, we choose only one station as the virtual source to invert for the Rayleigh wave phase velocity at 25 s. The NN hyperparameters are kept the same as those used in the field data training with multiple sources. Traditional ambient noise eikonal tomography is applied to the same data, utilizing the same source for direct comparison of phase velocity models and evaluation of methodology resolution. The velocity results in the vicinity of the source are unreliable due to the ambiguity between overlapping causal and anti-causal empirical Green's functions close to the source. Thus the data points with a region of 1.6° around the source location are removed from both results.

Figure 9a illustrates the phase velocity result for a single source recovered by pinnEAET while Figure 9b demonstrates that retrieved by conventional eikonal tomography. Both results show the main low velocity zones along the Qilian Orogenic Belt, Western Qinling Orogen and Songpan-Ganzi Terrane. The result from pinnEAET is closer to that of others utilizing all stations. It well recovers the majority of velocity structures except for some areas where path coverage is extremely limited. The result using conventional eikonal tomography displays many spurious velocity anomaly patterns and obvious smearing phenomena. It is clear that the results of pinnEAET show a more accurate solution compared to these earlier studies. The performance test gives support to the ability of our approach especially when the available data are limited.

5. Conclusion

We have developed a deep learning method for anisotropic ambient noise tomography based on physics-informed neural networks. By integrating physics constraints into the architecture, these models can effectively capture the underlying physics of the elliptical-anisotropic eikonal tomography problem. This method is designed to achieve high accuracy and robust results even with limited data and noisy input. We apply this approach to the Rayleigh wave correlation traveltime data recorded by a dense seismic array deployed on the northeastern Tibetan Plateau. The algorithm enables the simultaneous training of multiple periods of traveltime by setting the period as training data. The results can be achieved with comparable resolution as conventional methods using only 20 source stations, minimizing necessary data and memory requirements. We also show that our method still performs well when using extremely limited data and is able to resolve structure better than traditional eikonal topography. Anisotropy fast directions can be well resolved and are in agreement with existing fault zone structure. Overall, we show that elliptical-anisotropy eikonal tomography based on physics-informed neural networks is a competitive alternative to traditional methods to extract anisotropic velocity information from Rayleigh wave data.

Data Availability Statement

The traveltime data sets from ambient noise cross-correlations used in this study and the Rayleigh wave azimuthal anisotropic phase velocity models can be downloaded at Chen (2023): https://doi.org/10.5281/zenodo.8088610.

References

Aki, K., & Richards, P. G. (2002). Quantitative seismology.

Alkhalifah, T., Song, C., Waheed, U., & Hao, Q. (2020). Wavefield solutions from machine learned functions that approximately satisfy the wave equation. In *EAGE 2020 annual conference & exhibition online* (pp. 1–5).

Araya-Polo, M., Jennings, J., Adler, A., & Dahlke, T. (2018). Deep-learning tomography. *The Leading Edge*, *37*(1), 58–66. https://doi.org/10.1190/tle37010058.1

Baydin, A. G., Pearlmutter, B. A., Radul, A. A., & Siskind, J. M. (2018). Automatic differentiation in machine learning: A survey. *Journal of Machine Learning Research*, *18*, 1–43.

Becker, T. W., Lebedev, S., & Long, M. (2012). On the relationship between azimuthal anisotropy from shear wave splitting and surface wave tomography. *Journal of Geophysical Research*, *117*(B1), B01306. https://doi.org/10.1029/2011jb008705

Bensen, G., Ritzwoller, M., Barmin, M., Levshin, A. L., Lin, F., Moschetti, M., et al. (2007). Processing seismic ambient noise data to obtain reliable broad-band surface wave dispersion measurements. *Geophysical Journal International*, *169*(3), 1239–1260. https://doi.org/10.1111/j.1365-246x.2007.03374.x

Cao, F., Liang, C., Zhou, L., & Zhu, J. (2020). Seismic azimuthal anisotropy for the southeastern Tibetan plateau extracted by wave gradiometry analysis. *Journal of Geophysical Research: Solid Earth*, *125*(5), e2019JB018395. https://doi.org/10.1029/2019jb018395

Chen, Y. (2023). Physics-informed neural networks for elliptical-anisotropy eikonal tomography: Application to data from the northeastern Tibetan Plateau. https://doi.org/10.5281/zenodo.8088610

Chen, Y., De Ridder, S., Rost, S., Guo, Z., Wu, X., & Chen, Y. (2022). Eikonal tomography with physics-informed neural networks: Rayleigh wave phase velocity in the northeastern margin of the Tibetan Plateau. *Geophysical Research Letters*, *49*(21), e2022GL099053. https://doi.org/10.1029/2022gl099053

Clark, M. K., & Royden, L. H. (2000). Topographic ooze: Building the eastern margin of Tibet by lower crustal flow. *Geology*, *28*(8), 703–706. https://doi.org/10.1130/0091-7613(2000)28<703:tobtem>2.0.co;2

Crampin, S., & Booth, D. C. (1985). Shear-wave polarizations near the North Anatolian Fault–II. Interpretation in terms of crack-induced anisotropy. *Geophysical Journal International*, *83*(1), 75–92. https://doi.org/10.1111/j.1365-246x.1985.tb05157.x

Creasy, N., Pisconti, A., Long, M. D., Thomas, C., & Wookey, J. (2019). Constraining lowermost mantle anisotropy with body waves: A synthetic modelling study. *Geophysical Journal International*, *217*(2), 766–783. https://doi.org/10.1093/gji/ggz049

De Ridder, S., Biondi, B., & Nichols, D. (2015). Elliptical-anisotropic eikonal phase velocity tomography. *Geophysical Research Letters*, *42*(3), 758–764. https://doi.org/10.1002/2014gl062805

De Ridder, S., & Curtis, A. (2017). Seismic gradiometry using ambient seismic noise in an anisotropic Earth. *Geophysical Journal International*, *209*(2), 1168–1179. https://doi.org/10.1093/gji/ggx073

Ekström, G. (2011). A global model of Love and Rayleigh surface wave dispersion and anisotropy, 25–250 s. *Geophysical Journal International*, *187*(3), 1668–1686. https://doi.org/10.1111/j.1365-246x.2011.05225.x

England, P., & Houseman, G. (1986). Finite strain calculations of continental deformation: 2. Comparison with the India-Asia collision zone. *Journal of Geophysical Research*, *91*(B3), 3664–3676. https://doi.org/10.1029/jb091ib03p03664

Fang, Z., & Zhan, J. (2019). Deep physical informed neural networks for metamaterial design. *IEEE Access*, *8*, 24506–24513. https://doi.org/10.1109/access.2019.2963375

Gao, Y., Shi, Y., & Wang, Q. (2020). Seismic anisotropy in the southeastern margin of the Tibetan Plateau and its deep tectonic significances. *Chinese Journal of Geophysics*, *63*(3), 802–816.

Gou, R., Zhang, Y., & Zhu, X. (2022). Bayesian physics-informed neural networks for seismic tomography based on the eikonal equation. arXiv preprint arXiv:2203.12351.

Haghighat, E., & Juanes, R. (2021). SciANN: A Keras/TensorFlow wrapper for scientific computations and physics-informed deep learning using artificial neural networks. *Computer Methods in Applied Mechanics and Engineering*, *373*, 113552. https://doi.org/10.1016/j.cma.2020.113552

Hao, S., Huang, Z., Han, C., Wang, L., Xu, M., Mi, N., & Yu, D. (2021). Layered crustal azimuthal anisotropy beneath the northeastern Tibetan Plateau revealed by Rayleigh-wave eikonal tomography. *Earth and Planetary Science Letters*, *563*, 116891. https://doi.org/10.1016/j.epsl.2021.116891

Ho, M., Idgunji, S., Payne, J. L., & Koeshidayatullah, A. (2023). Hierarchical multi-label taxonomic classification of carbonate skeletal grains with deep learning. *Sedimentary Geology*, *443*, 106298. https://doi.org/10.1016/j.sedgeo.2022.106298

Karimpouli, S., & Tahmasebi, P. (2020). Physics informed machine learning: Seismic wave equation. *Geoscience Frontiers*, *11*(6), 1993–2001. https://doi.org/10.1016/j.gsf.2020.07.007

Karpatne, A., Atluri, G., Faghmous, J. H., Steinbach, M., Banerjee, A., Ganguly, A., et al. (2017). Theory-guided data science: A new paradigm for scientific discovery from data. *IEEE Transactions on Knowledge and Data Engineering*, *29*(10), 2318–2331. https://doi.org/10.1109/tkde.2017.2720168

Kästle, E. D., Molinari, I., Boschi, L., Kissling, E., & Group, A. W. (2022). Azimuthal anisotropy from eikonal tomography: Example from ambient-noise measurements in the AlpArray network. *Geophysical Journal International*, *229*(1), 151–170. https://doi.org/10.1093/gji/ggab453

Kim, Y., & Yun, T. S. (2021). How to classify sand types: A deep learning approach. *Engineering Geology*, *288*, 106142. https://doi.org/10.1016/j.enggeo.2021.106142

Kingma, D. P., & Ba, J. (2014). Adam: A method for stochastic optimization. arXiv preprint arXiv:1412.6980.

Kissas, G., Yang, Y., Hwuang, E., Witschey, W. R., Detre, J. A., & Perdikaris, P. (2020). Machine learning in cardiovascular flows modeling: Predicting arterial blood pressure from non-invasive 4D flow MRI data using physics-informed neural networks. *Computer Methods in Applied Mechanics and Engineering*, *358*, 112623. https://doi.org/10.1016/j.cma.2019.112623

Li, S., Guo, Z., Yu, Y., Wu, X., & Chen, Y. J. (2022). Imaging the Northeastern crustal boundary of the Tibetan Plateau with radial anisotropy. *Geophysical Research Letters*, *49*(23), e2022GL100672. https://doi.org/10.1029/2022gl100672

Li, S., Xiong, L., Tang, G., & Strobl, J. (2020). Deep learning-based approach for landform classification from integrated data sources of digital elevation model and imagery. *Geomorphology*, *354*, 107045. https://doi.org/10.1016/j.geomorph.2020.107045

Li, Y., Pan, J., Wu, Q., & Ding, Z. (2017). Lithospheric structure beneath the northeastern Tibetan Plateau and the western Sino-Korea Craton revealed by Rayleigh wave tomography. *Geophysical Journal International*, *210*(2), 570–584. https://doi.org/10.1093/gji/ggx181

Li, Y., Wu, Q., Zhang, F., Feng, Q., & Zhang, R. (2011). Seismic anisotropy of the Northeastern Tibetan Plateau from shear wave splitting analysis. *Earth and Planetary Science Letters*, *304*(1–2), 147–157. https://doi.org/10.1016/j.epsl.2011.01.026

Lin, F.-C., Moschetti, M. P., & Ritzwoller, M. H. (2008). Surface wave tomography of the western United States from ambient seismic noise: Rayleigh and Love wave phase velocity maps. *Geophysical Journal International*, *173*(1), 281–298. https://doi.org/10.1111/j.1365-246x.2008.03720.x

Lin, F.-C., & Ritzwoller, M. H. (2011). Helmholtz surface wave tomography for isotropic and azimuthally anisotropic structure. *Geophysical Journal International*, *186*(3), 1104–1120. https://doi.org/10.1111/j.1365-246x.2011.05070.x

Lin, F.-C., Ritzwoller, M. H., & Snieder, R. (2009). Eikonal tomography: Surface wave tomography by phase front tracking across a regional broad-band seismic array. *Geophysical Journal International*, *177*(3), 1091–1110. https://doi.org/10.1111/j.1365-246x.2009.04105.x

Lobkis, O. I., & Weaver, R. L. (2001). On the emergence of the Green's function in the correlations of a diffuse field. *Journal of the Acoustical Society of America*, *110*(6), 3011–3017. https://doi.org/10.1121/1.1417528

Long, M. D., & Becker, T. W. (2010). Mantle dynamics and seismic anisotropy. *Earth and Planetary Science Letters*, *297*(3–4), 341–354. https://doi.org/10.1016/j.epsl.2010.06.036

Luo, Z., Xiong, Y., & Zuo, R. (2020). Recognition of geochemical anomalies using a deep variational autoencoder network. *Applied Geochemistry*, *122*, 104710. https://doi.org/10.1016/j.apgeochem.2020.104710

Misyris, G. S., Venzke, A., & Chatzivasileiadis, S. (2020). Physics-informed neural networks for power systems. In *2020 IEEE power & energy society general meeting (PESGM)* (pp. 1–5).

Molnar, P., & Tapponnier, P. (1975). Cenozoic Tectonics of Asia: Effects of a Continental Collision: Features of recent continental tectonics in Asia can be interpreted as results of the India-Eurasia collision. *Science*, *189*(4201), 419–426. https://doi.org/10.1126/science.189.4201.419

Montagner, J. (1986). Regional three-dimensional structures using long-period surface waves. *Annales Geophysicae*, *4*(B3), 283–294.

Montagner, J.-P., & Guillot, L. (2002). Seismic anisotropy and global geodynamics. *Reviews in Mineralogy and Geochemistry*, *51*(1), 353–385. https://doi.org/10.2138/gsrmg.51.1.353

Moseley, B., Markham, A., & Nissen-Meyer, T. (2020). Solving the wave equation with physics-informed deep learning. arXiv preprint arXiv:2006.11894.

Moseley, B., Nissen-Meyer, T., & Markham, A. (2020). Deep learning for fast simulation of seismic waves in complex media. *Solid Earth*, *11*(4), 1527–1549. https://doi.org/10.5194/se-11-1527-2020

Mousavi, S. M., Ellsworth, W. L., Zhu, W., Chuang, L. Y., & Beroza, G. C. (2020). Earthquake transformer—An attentive deep-learning model for simultaneous earthquake detection and phase picking. *Nature Communications*, *11*(1), 1–12. https://doi.org/10.1038/s41467-020-17591-w

Nicolas, A., & Christensen, N. I. (1987). Formation of anisotropy in upper mantle peridotites-A review. *Composition, structure and dynamics of the lithosphere-asthenosphere system*, *16*, 111–123.

Raissi, M., Perdikaris, P., & Karniadakis, G. E. (2019). Physics-informed neural networks: A deep learning framework for solving forward and inverse problems involving nonlinear partial differential equations. *Journal of Computational Physics*, *378*, 686–707. https://doi.org/10.1016/j.jcp.2018.10.045

Raissi, M., Yazdani, A., & Karniadakis, G. E. (2020). Hidden fluid mechanics: Learning velocity and pressure fields from flow visualizations. *Science*, *367*(6481), 1026–1030. https://doi.org/10.1126/science.aaw4741

Rasht-Behesht, M., Huber, C., Shukla, K., & Karniadakis, G. E. (2022). Physics-informed neural networks (PINNs) for wave propagation and full waveform inversions. *Journal of Geophysical Research: Solid Earth*, *127*(5), e2021JB023120. https://doi.org/10.1029/2021jb023120

Ritzwoller, M. H., Lin, F.-C., & Shen, W. (2011). Ambient noise tomography with a large seismic array. *Comptes Rendus Geoscience*, *343*(8–9), 558–570. https://doi.org/10.1016/j.crte.2011.03.007

Romanowicz, B. (2002). Inversion of surface waves: A review. *International Geophysics Series*, *81*(A), 149–174.

Ross, Z. E., Meier, M.-A., & Hauksson, E. (2018). P wave arrival picking and first-motion polarity determination with deep learning. *Journal of Geophysical Research: Solid Earth*, *123*(6), 5120–5129. https://doi.org/10.1029/2017jb015251

Royden, L. H., Burchfiel, B. C., King, R. W., Wang, E., Chen, Z., Shen, F., & Liu, Y. (1997). Surface deformation and lower crustal flow in eastern Tibet. *Science*, *276*(5313), 788–790. https://doi.org/10.1126/science.276.5313.788

Russell, J. B., Gaherty, J. B., Lin, P.-Y. P., Lizarralde, D., Collins, J. A., Hirth, G., & Evans, R. L. (2019). High-resolution constraints on Pacific upper mantle petrofabric inferred from surface-wave anisotropy. *Journal of Geophysical Research: Solid Earth*, *124*(1), 631–657. https://doi.org/10.1029/2018jb016598

Savage, M. (1999). Seismic anisotropy and mantle deformation: What have we learned from shear wave splitting? *Reviews of Geophysics*, *37*(1), 65–106. https://doi.org/10.1029/98rg02075

Schulte-Pelkum, V., & Mahan, K. H. (2014). A method for mapping crustal deformation and anisotropy with receiver functions and first results from USArray. *Earth and Planetary Science Letters*, *402*, 221–233. https://doi.org/10.1016/j.epsl.2014.01.050

Sethian, J. A. (1999). Fast marching methods. *SIAM Review*, *41*(2), 199–235. https://doi.org/10.1137/s0036144598347059

Shapiro, N. M., Campillo, M., Stehly, L., & Ritzwoller, M. H. (2005). High-resolution surface-wave tomography from ambient seismic noise. *Science*, *307*(5715), 1615–1618. https://doi.org/10.1126/science.1108339

Silver, P. G. (1996). Seismic anisotropy beneath the continents: Probing the depths of geology. *Annual Review of Earth and Planetary Sciences*, *24*(1), 385–432. https://doi.org/10.1146/annurev.earth.24.1.385

Simons, F. J., Van Der Hilst, R. D., Montagner, J.-P., & Zielhuis, A. (2002). Multimode Rayleigh wave inversion for heterogeneity and azimuthal anisotropy of the Australian upper mantle. *Geophysical Journal International*, *151*(3), 738–754. https://doi.org/10.1046/j.1365-246x.2002.01787.x

Smith, J. D., Azizzadenesheli, K., & Ross, Z. E. (2020). Eikonet: Solving the eikonal equation with deep neural networks. *IEEE Transactions on Geoscience and Remote Sensing*, *59*(12), 10685–10696. https://doi.org/10.1109/tgrs.2020.3039165

Smith, M. L., & Dahlen, F. (1973). The azimuthal dependence of Love and Rayleigh wave propagation in a slightly anisotropic medium. *Journal of Geophysical Research*, *78*(17), 3321–3333. https://doi.org/10.1029/jb078i017p03321

Soergel, D., Pedersen, H. A., Bodin, T., Paul, A., Stehly, L., Hetényi, G., et al. (2023). Bayesian analysis of azimuthal anisotropy in the alpine lithosphere from beamforming of ambient noise cross-correlations. *Geophysical Journal International*, *232*(1), 429–450. https://doi.org/10.1093/gji/ggac349

Song, C., Alkhalifah, T., & Waheed, U. (2021). Solving the frequency-domain acoustic vti wave equation using physics-informed neural networks. *Geophysical Journal International*, *225*(2), 846–859. https://doi.org/10.1093/gji/ggab010

Song, C., Alkhalifah, T., & Waheed, U. (2022). A versatile framework to solve the Helmholtz equation using physics-informed neural networks. *Geophysical Journal International*, *228*(3), 1750–1762. https://doi.org/10.1093/gji/ggab434

Song, C., & Alkhalifah, T. A. (2021). Wavefield reconstruction inversion via physics-informed neural networks. *IEEE Transactions on Geoscience and Remote Sensing*, *60*, 1–12. https://doi.org/10.1109/tgrs.2021.3123122

Song, C., & Wang, Y. (2023). Simulating seismic multifrequency wavefields with the Fourier feature physics-informed neural network. *Geophysical Journal International*, *232*(3), 1503–1514. https://doi.org/10.1093/gji/ggac399

Tapponnier, P., Zhiqin, X., Roger, F., Meyer, B., Arnaud, N., Wittlinger, G., & Jingsui, Y. (2001). Oblique stepwise rise and growth of the Tibet Plateau. *Science*, *294*(5547), 1671–1677. https://doi.org/10.1126/science.105978

Taufik, M. H., Waheed, U., & Alkhalifah, T. A. (2022). Upwind, no more: Flexible traveltime solutions using physics-informed neural networks. *IEEE Transactions on Geoscience and Remote Sensing*, *60*, 1–12. https://doi.org/10.1109/tgrs.2022.3218754

Treister, E., & Haber, E. (2016). A fast marching algorithm for the factored eikonal equation. *Journal of Computational Physics*, *324*, 210–225. https://doi.org/10.1016/j.jcp.2016.08.012

Waheed, U., Alkhalifah, T., Haghighat, E., Song, C., & Virieux, J. (2021). Pinntomo: Seismic tomography using physics-informed neural networks. arXiv preprint arXiv:2104.01588.

Waheed, U., Haghighat, E., & Alkhalifah, T. (2020). Anisotropic eikonal solution using physics-informed neural networks. In *SEG international exposition and annual meeting*.

Waheed, U., Haghighat, E., Alkhalifah, T., Song, C., & Hao, Q. (2021). PINNeik: Eikonal solution using physics-informed neural networks. *Computers & Geosciences*, *155*, 104833. https://doi.org/10.1016/j.cageo.2021.104833

Wang, K., Lu, L., Maupin, V., Ding, Z., Zheng, C., & Zhong, S. (2020). Surface wave tomography of Northeastern Tibetan Plateau using beamforming of seismic noise at a dense array. *Journal of Geophysical Research: Solid Earth*, *125*(4), e2019JB018416. https://doi.org/10.1029/2019jb018416

Wang, X., Li, Y., Ding, Z., Zhu, L., Wang, C., Bao, X., & Wu, Y. (2017). Three-dimensional lithospheric S wave velocity model of the NE Tibetan Plateau and western North China Craton. *Journal of Geophysical Research: Solid Earth*, *122*(8), 6703–6720. https://doi.org/10.1002/2017jb014203

Wapenaar, K. (2004). Retrieving the elastodynamic Green's function of an arbitrary inhomogeneous medium by cross correlation. *Physical Review Letters*, *93*(25), 254301. https://doi.org/10.1103/physrevlett.93.254301

Wapenaar, K., Draganov, D., Snieder, R., Campman, X., & Verdel, A. (2010). Tutorial on seismic interferometry: Part 1—Basic principles and applications. *Geophysics*, *75*(5), 75A195–75A209. https://doi.org/10.1190/1.3457445

Weisstein, E. W. (2014). Ellipse. From MathWorld–a wolfram web resource. Retrieved from https://mathworld.wolfram.com/Ellipse.html

Wu, X., Guo, Z., Li, S., Yu, Y., Bai, Q., & Chen, Y. J. (2023). Seismic azimuthal anisotropy of northeastern Tibetan Plateau from ambient noise double beamforming tomography: Implication for crustal deformation. *Journal of Geophysical Research: Solid Earth*, *128*(6), e2022JB026109. https://doi.org/10.1029/2022jb026109

Yang, F., & Ma, J. (2019). Deep-learning inversion: A next-generation seismic velocity model building method. *Geophysics*, *84*(4), R583–R599. https://doi.org/10.1190/geo2018-0249.1

Yao, H., Van Der Hilst, R. D., & Montagner, J.-P. (2010). Heterogeneity and anisotropy of the lithosphere of SE Tibet from surface wave array tomography. *Journal of Geophysical Research*, *115*(B12), B12307. https://doi.org/10.1029/2009jb007142

Yin, A., & Harrison, T. M. (2000). Geologic evolution of the Himalayan-Tibetan orogen. *Annual Review of Earth and Planetary Sciences*, *28*(1), 211–280. https://doi.org/10.1146/annurev.earth.28.1.211

Yu, S., & Ma, J. (2021). Deep learning for geophysics: Current and future trends. *Reviews of Geophysics*, *59*(3), e2021RG000742. https://doi.org/10.1029/2021rg000742

Zhang, C., Guo, Z., & Chen, Y. J. (2020). Lithospheric thickening controls the ongoing growth of northeastern Tibetan Plateau: Evidence from p and s receiver functions. *Geophysical Research Letters*, *47*(15), e2020GL088972. https://doi.org/10.1029/2020gl088972

Zhao, D., Yu, S., & Liu, X. (2016). Seismic anisotropy tomography: New insight into subduction dynamics. *Gondwana Research*, *33*, 24–43. https://doi.org/10.1016/j.gr.2015.05.008

Zheng, T., Gao, S. S., Ding, Z., Liu, K. H., Chang, L., Fan, X., et al. (2021). Crustal azimuthal anisotropy and deformation beneath the northeastern Tibetan Plateau and adjacent areas: Insights from receiver function analysis. *Tectonophysics*, *816*, 229014. https://doi.org/10.1016/j.tecto.2021.229014

Zhu, W., Mousavi, S. M., & Beroza, G. C. (2019). Seismic signal denoising and decomposition using deep neural networks. *IEEE Transactions on Geoscience and Remote Sensing*, *57*(11), 9476–9488. https://doi.org/10.1109/tgrs.2019.2926772